

A convolutional autoencoder approach for mining features in cellular electron cryo-tomograms and weakly supervised coarse segmentation

Xiangrui Zeng¹, Miguel Ricardo Leung², Tzviya Zeev-Ben-Mordehai², and Min Xu^{*1}

¹Computational Biology Department, School of Computer Science, Carnegie Mellon University, Pittsburgh, 15213, USA

²Division of Structural Biology, Wellcome Trust Centre for Human Genetics, University of Oxford, Oxford, OX3 7BN, UK

Abstract

Cellular electron cryo-tomography enables the 3D visualization of cellular organization in a near-native state at submolecular resolution. However, the content of a cellular tomogram is often complex, making it difficult to automatically isolate different *in situ* cellular components. In this paper, we propose a convolutional autoencoder-based unsupervised approach to provide a coarse characterization of 3D patches extracted from tomograms. We demonstrate that the autoencoder can be used for the efficient and coarse characterizing of features that correspond to macromolecular complexes and surfaces, like membranes. In addition, it can be used to detect non-cellular features related to sample preparation and data collection like carbon edges from the grid, and tomogram boundaries. The autoencoder is also able to detect patterns that may indicate spatial interactions between cell components. Furthermore, we demonstrate that our autoencoder can be used for weakly supervised semantic segmentation of cellular components requiring very small amount of manual annotation.

1 Introduction

Recent developments in cellular electron cryo-tomography (CECT) now enable the 3D visualization of cellular organization at submolecular resolution in a near-native state. At this resolution, subcellular components can be systematically analyzed at unprecedented levels of detail. The 3D visualization *in situ* has made possible the discovery of numerous important structural features in both prokaryotic and eukaryotic cells as well as in viruses [17, 7, 14, 18]. As CECT develops, high quality data produced by this approach continues to yield valuable insights into the structural organization of the cell.

In principle, a tomogram of a cell contains structural information of all cellular components within the field of view. However, given that cellular structures are packed within a small volume at high density, an important problem that CECT continues to grapple with is how to systemically extract cellular structural information. This is due in part to the crowded nature of these intracellular structures. In addition, imaging limits, including low signal to noise ratio (SNR) and missing wedge effects further increase the difficulty of systematic recovery of such information. Currently, many CECT structural identification / characterization and segmentation tasks are performed by visual inspection and manual labeling / annotation, which can be very laborious. Consequently, the labor-intensive nature of these analyses has become a bottleneck for CECT studies.

Particle structural separation approaches may be used for systematic automatic characterization of structural or image features. A particle is represented as a *subtomogram*, which is an image patch of cubic shape. Reference-free subtomogram classification [e.g. 5, 40, 11, 37] and *de novo* structural pattern mining [44] have

*Corresponding author email: mxu1@cs.cmu.edu

been developed for structural separation of particles. Nevertheless, such approaches are designed for recovering structures of large macromolecular complexes. The steps for subtomogram alignment or integration over all rigid transformations in those approaches are very computationally intensive, therefore limited their scalability. To increase scalability, we and others have developed 3D rotational invariant feature [41, 42, 10] and pose normalization [44] approaches. However, they are limited to subtomograms whose shapes are cubic to allow rotation operations. Recently, we developed a supervised deep structural feature extraction approach [43] that can be used for characterization of structural or image features. Nevertheless, this method employs a supervised approach that relies on training using annotated data.

In this paper, we complement existing approaches by developing an unsupervised approach for automatic characterization of tomogram features. Automatic characterization of image features (represented as 3D image patches) is very useful for separating heterogeneous image patches into homogeneous image patch sets. Unlike subtomograms, 3D image patches are small sub-volumes extracted from a tomogram whose shape does not necessarily have to be cubic. Such homogeneous sets of image patches is useful to simplify the structural mining process by separating structures with different shapes or orientations. Although resulting image patch sets are not labeled, image feature clues are provided to guide the identification of representative structures. Unknown structures of the same type and orientation are likely to be clustered in the same image patch set, which helps the identification of the structure and spatial organization in a systematic fashion.

Specifically, we propose a 3D convolutional autoencoder model for efficient unsupervised encoding image features (Figure 1a). A convolutional autoencoder is a type of Convolutional Neural Network (CNN) designed for unsupervised deep learning. The convolution layers are used for automatic extraction of an image feature hierarchy. The training of the autoencoder encodes image features (represented as 3D image patches) into compressed representations. The encoded image features are clustered using k-means clustering. An image patch set is then characterized by the decoded cluster center. With the omission of the image rotation operation, and with GPU acceleration, the separation process is significantly more scalable than the subtomogram classification [e.g. 40] and pattern mining [44] approaches. As a result, it is particularly suitable for unsupervised structural mining among large amounts of image patches and identifying representative structures with representative orientations. Through testing our approach on experimental cellular cryo-tomograms, we are able to efficiently encode and cluster tens of thousands of image patches using a single GPU. We identified 1) surface features such as membranes, carbon edges, and tomogram boundaries of certain orientations and 2) large globular features corresponding to macromolecular complexes likely to be ribosomes. Both the surface features and the large globular features were validated by embedding these patterns back into the tomograms. We further identified a spatial interaction pattern between cellular components, which is not straightforward to identify through visual inspection.

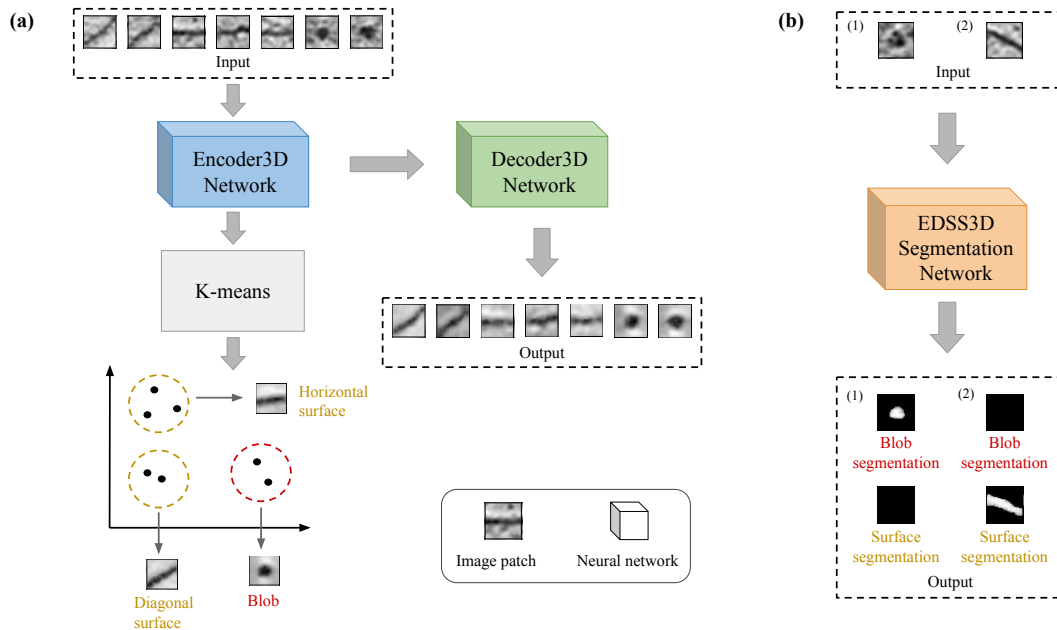


Figure 1: (a) Autoencoder for characterization of image patches (Section 2.2). (b) Encoder-decoder network for image patch semantic segmentation (Section 2.4).

Manual segmentation of 2D images is laborious, manual segmentation of tomograms is even more so. To facilitate structural segmentation, automatic or semi-automatic approaches have been developed for segmenting specific structures. Such approaches use manually designed rules for 1) extraction of image features characterizing the specific ultrastructure and 2) segmentation based on combinations of extracted image features. All feature extraction and segmentation rules are specifically designed for particular types of image features or ultrastructures, such as membrane [e.g. 6, 27, 28, 13] and actin filaments [36, 45]. However, only very few generic and unified approaches exist for segmenting various structures [e.g. 9, 26]. Generic and unified approaches come with the advantage of being easily extended to segmenting new types of structures through automatic learning rules instead of manually designing them. The learning of rules is often done through a supervised fashion. In recent years, deep learning based approaches [e.g. 25] emerge as the dominant approaches for supervised generic segmentation in computer vision applications due to its superior performance in the presence of large amount of training data. Recently, deep learning has also been used for generic segmentation of ultrastructures [9] in cellular tomograms. Supervised segmentation approaches often rely on training data prepared through manual segmentation of images. Manual segmentation of tomograms is a voxel level annotation, and can be very laborious. Therefore, it is beneficial to develop approaches to reduce the amount of supervision (in terms of manual annotation) to speed up the automation of training data preparation.

To complement existing approaches through reducing the amount of supervision, here we further demonstrate that the cluster groups generated from our autoencoder can be used to train a 3D CNN model for semantic segmentation in a weakly supervised fashion. In particular, after simple manual selection and grouping the clusters, the groups of clusters are used to train dense classifiers for voxel level classification for supervised (semantic) segmentation of tomograms. In the whole segmentation pipeline, the laborious manual voxel-wise segmentation of 3D images is no longer needed. The only step that require manual intervention is manual selection and grouping of image feature clusters among a number (such as 100) of candidate clusters, based on decoded cluster centers and location of the image features in the clusters. Therefore, the whole pipeline is weakly supervised with minimal manual processing. Our preliminary tests on experimental tomograms demonstrates the efficacy of our approach.

2 Methods

2.1 Background

Deep learning is one of the dominant computer vision techniques used today across a broad array of applications [22]. Specifically, Convolutional Neural Network (CNN) [23] has achieved high performance and accuracy in computer vision tasks such as image classification [21] and semantic segmentation [25]. CNN is a feedforward artificial neural network inspired by the hierarchical organization of animal visual cortex. A CNN model is a combination of layers in sequence and each layer consists of a certain number of neurons with receptive fields on the previous layer.

The learnable unit of each layer, called a neuron, connects with part of a previous layer, called a receptive field or filter. For example, a 1D convolution of input \mathbf{x} , output \mathbf{y} , and filter size $2m + 1$ is defined as $\mathbf{y}_i = \sum_{j=-m}^m \mathbf{w}_j \mathbf{x}_{i-j}$, where \mathbf{w}_j is the j th weight of the convolutional filter. The weight of a neuron is updated after every training epoch based on the loss of the prediction.

There exists different types of CNN layers: convolutional layer, fully connected layer, up sampling layer, pooling layer, etc. A convolutional layer is defined as a layer with neurons of certain filter sizes. A fully connected layer is a layer in which every neuron is connected to every neuron in the previous layer. A pooling layer is a type of non-linear down sampling layer to reduce the spatial representation size. Such pooling often outputs the local maximum (max pooling) or average (average pooling) of its receptive field. For example, a 1D max pooling of input \mathbf{x} , output \mathbf{y} , and pooling size m is defined as $\mathbf{y}_i = \max_{(i-1)m < j \leq im} \mathbf{x}_j$. Similarly, an up sampling layer is to increase the spatial representation size by repeating the number in the receptive field. For example, a 1D up sampling of input \mathbf{x} , output \mathbf{y} , and up sampling size $m + 1$ is defined as $\mathbf{y}_{i-j} = \mathbf{x}_j$, where \mathbf{y}_{i-j} is the i to j th output and $i + m = j$.

Following a convolution, an activation function such as a rectified liner unit (ReLU) [30] is applied. The ReLU activation is defined as $\sigma^{ReLU}(\mathbf{x}) = \max\{\mathbf{0}, \mathbf{x}\}$. ReLU activation has the advantage of being sparse, scale invariant, and simple enough for efficient computation and gradient propagation.

For an autoencoder network, the output reconstructs the input. Because both the input and output consist of continuous real values, the final output layer is usually a linear activation layer. The linear activation is defined as $\sigma^{linear}(\mathbf{x}) = \mathbf{x}$, which is simple to compute and favored when the output is composed of unbounded continuous values. Semantic segmentation is one type of multi-class classification tasks where an image is partitioned into semantically meaningful parts and each part is classified into one of the pre-defined classes. Softmax activation is usually applied as the last output layer for classification tasks. The softmax activation is defined as:

$$\sigma_j^{softmax}(\mathbf{x}) = P(j|\mathbf{x}) = \frac{e^{\mathbf{x}^T \mathbf{w}_j}}{\sum_{l=1}^L e^{\mathbf{x}^T \mathbf{w}_l}}$$

where \mathbf{x} is the input of the last layer and \mathbf{w}_j is the weight associated with the j th class. The softmax activation calculates the probability $P(j|\mathbf{x})$ of a sample being classified into each class. In the 3D image semantic segmentation task, each voxel is treated as a sample and a semantic class label is assigned to each voxel.

A CNN model is trained to optimize the weight of each neuron in its layer through backpropagation in conjugation with a optimization method. After being provided with training data of paired inputs and outputs, backpropagation works by propagating forward the input through the network and compares the output with the true output via a loss function. The error of each neuron in the output layer is calculated and propagates backward to calculate gradient of the loss function with respect to each neuron's weight. Then the weights are updated for next training phase. Gradient descent methods are the most common optimization methods [16] because of their computational simplicity.

2.2 Autoencoder3D network for unsupervised image feature characterization

A typical autoencoder [16] consists of two main components, the encoder $\phi: \mathbf{X} \rightarrow \mathbf{F}$, which encodes the input \mathbf{X} to a representation \mathbf{F} , usually of lower dimensions, and the decoder $\psi: \mathbf{F} \rightarrow \hat{\mathbf{X}}$, which decodes the representation \mathbf{F} to a reconstruction of \mathbf{X} , $\hat{\mathbf{X}}$. Autoencoder network is trained to minimize the distance between input \mathbf{X} and reconstruction output $\hat{\mathbf{X}}$. Normally, the goal of Autoencoder network is to reduce the dimension of input and characterize representative features with high precision.

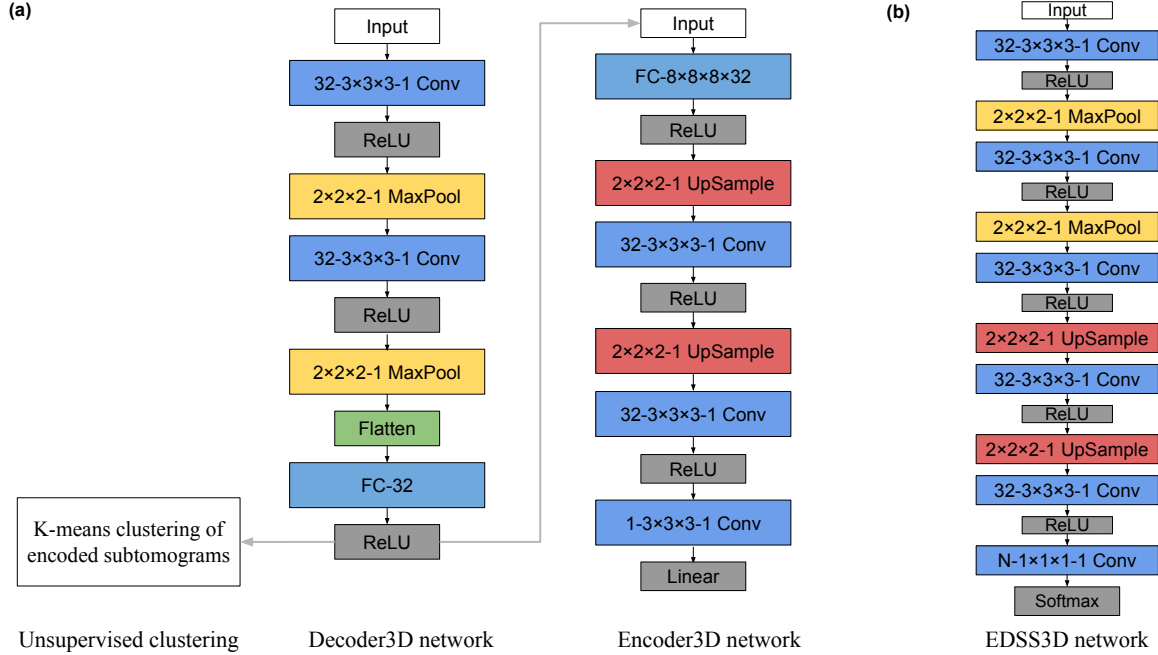


Figure 2: Architecture of our CNN models. All three networks have multiple layers. Each colored box represents one layer and lists its type and configuration. For example, ‘32 – 3 × 3 × 3 – 1 Conv’ denotes a 3D convolutional layer with 32 filters, 3 × 3 × 3 kernel size and 1 stride. ‘2 × 2 × 2 – 1 MaxPool or UpSample’ denotes a 3D max pooling or up sampling layer over a 2 × 2 × 2 region with 1 stride, respectively. ‘FC-8 × 8 × 8 × 32’ denotes a fully connected layer with neurons of dimensionality 8 × 8 × 8 × 32, where every neuron is connected to every output of previous layer. ‘Flatten’ denotes a layer that flattens the input. N is the number of classes in the semantic segmentation training set. ‘ReLU’, ‘Linear’, ‘Softmax’ denote different types of activation layers.

We propose a 3D convolutional autoencoder model, denoted as Autoencoder3D. The input of Autoencoder3D network is a 3D image patch extracted from a tomogram, represented as a 3D array \mathbf{A} of $R^{m \times n \times p}$. Since our method does not require rotation of such an image patch, the shape of input image patches needs not necessarily to be cubic. The Encoder3D network encodes the image patch \mathbf{A} as an encoding vector \mathbf{v} of R^{32} . The Decoder3D network decodes the encoding vector \mathbf{v} to a reconstruction $\hat{\mathbf{A}}$ of the same size $R^{m \times n \times p}$.

The architecture of the Autoencoder3D model is shown in Figure 2a. The Encoder3D part contains two convolutional layers with 3 × 3 × 3 3D filters, two 2 × 2 × 2 3D max pooling layers, and one fully connected output layer outputting vector \mathbf{v} of length 32. We use $L1$ norm regularization to encourage sparsity in the encoded features. Previous work [31] shows that sparsity regularization improves autoencoder performance. The Decoder3D part contains one fully connected layer with the same output shape as the input shape of the encoder3D fully connected output layer, two convolutional layers with 3 × 3 × 3 3D filters, two 2 × 2 × 2 3D up sampling layers, and one convolutional output layer with 3 × 3 × 3 3D filters. All hidden layers and the Encoder3D fully connected output layer are equipped with the rectified linear (ReLU) activation. The Decoder3D convolutional output layer is equipped with a linear activation.

2.3 Unsupervised learning for image patch grouping

Clustering is a necessary step for collecting homogeneous groups of image patches from heterogeneous inputs. However, the distance measures calculated directly on two image patches have limited ability to discriminate due to the difficulties associated with the dimensionality of the samples [43, 3]. Therefore, we propose an unsupervised image patch clustering approach based on encoded features of substantially lower numbers of dimensions. Using the Autoencoder3D network, each image patch is encoded into a vector of real numbers

that represent features of the original image patch. K-means clustering is then applied to group similar image patches together based on the encoding.

We note here that after the k-means clustering, a simple step of manually selecting interested clusters is needed for further supervised semantic segmentation of new datasets in Section 2.4. To do so, the decoded cluster centers are plotted to guide the user to select and group clusters of interest. Selected and grouped clusters are used as positive samples in a training dataset for training a semantic segmentation model defined in Section 2.4. An example of such selecting and semantic segmentation model training is described in 3.1.4 and 3.1.5. The segmentation used for training in the training set is obtained by thresholding the decoded 3D images at a certain mask level.

2.4 EDSS3D network for weakly supervised semantic segmentation

In this section, we propose a 3D encoder-decoder semantic segmentation network (EDSS3D) to perform supervised segmentation of new image patch data based on previous unsupervised learning results. The design of the model is inspired by [4]. The input of EDSS3D network is a 3D image patch, represented as a 3D array \mathbf{B} of $R^{m \times n \times p}$, extracted from a testing dataset tomogram. The EDSS3D network outputs \mathbf{L} number of 3D arrays \mathbf{B}'_l of the same size $R^{m \times n \times p}$, where \mathbf{L} is the number of semantic classes and each voxel in \mathbf{B}'_l denotes the segmentation probability of this voxel belonging to the l th semantic class.

In particular, the decoded 3D images of selected clusters are used as training data. The architecture of EDSS3D model is shown in Figure 2b. The architecture consists of five convolutional layers with $3 \times 3 \times 3$ 3D filters, two $2 \times 2 \times 2$ 3D max pooling layers, two $2 \times 2 \times 2$ 3D up sampling layers, and one convolutional 3D output layer with the number of filters equal to the number of segmentation classes. All hidden layers are equipped with ReLU activation layer. The convolutional 3D output layer is equipped with a softmax activation layer.

Similar to the Autoencoder3D model, our EDSS3D model is an encoder-decoder bottleneck-type model with same-size output as the input. However, Autoencoder3D model performs image encoding for unsupervised image feature characterization whereas EDSS3D model performs supervised image semantic segmentation. Accordingly, EDSS3D model does not break into two parts. The EDSS3D model has an output softmax activation layer rather than a linear activation layer for better multi-class classification performance.

2.5 Implementation details

The training and testing of our CNN models were implemented using Keras [12] and Tensorflow [2]. Image processing suite EMAN2 was used for reading tomograms [38]. A variant of our Tomominer library was used for data preparation and image display [15, 44]. K-means clustering was performed using the Sklearn toolbox [32]. Chimera [34] and Mayavi [35] were used to generate the embedded tomogram figures. The experiments were performed on a computer equipped with Nvidia GTX 1080 GPU, one Intel Core i5-5300U CPU, and 256 GB memory.

3 Results

3.1 Tests on COS-7 cells

3.1.1 Sample preparation and vitrification

COS-7 (*Cercopithecus aethiops* kidney) cells were grown on c-flat gold mesh carbon-coated holey carbon grids to a density of 1-2 cells/grid square. Cells were maintained in Dulbecco's modified Eagle's medium supplemented with L-Glutamine, nonessential amino acids, and 10% fetal bovine serum at 37°C, 5% CO₂. Prior to freezing, BSA-conjugated 10-nm gold fiducial markers were added to grids, which were then blotted manually from the backside of the grids for 4 s, and plunged into a liquid ethane/propane mixture cooled to liquid N₂ temperature.

3.1.2 Data acquisition

Cryo-electron microscopy was performed at 300 keV on a Tecnai TF30 “Polara” electron microscope equipped with a Quantum postcolumn energy filter (Gatan) operated in zero-loss imaging mode with a 20-eV energy-selecting slit. All images were recorded on a postfilter $\approx 4000 \times 4000$ K2-summit direct electron detector (Gatan) operated in counting mode with dose fractionation, with a calibrated pixel size of 0.355 nm at the specimen level. Tilt series were collected using SerialEM at a defocus of $-6 \mu\text{m}$. Tilt series covered an angular range of -60° to $+50^\circ$ in increments of 4° . Tomograms were reconstructed in IMOD using weighted back-projection. The resulting two tomograms were termed COS-7 tomogram 1 and COS-7 tomogram 2.

3.1.3 Data preparation and autoencoder training

To collect image patches, we performed a reference-free Difference of Gaussian (DoG) particle picking process as described in [33]. COS-7 tomogram 1 was convoluted with a Gaussian Kernel of $\sigma = 2$ voxels in radius for smoothing and then with a 3D DoG function with scaling factor of $\sigma = 5$ voxels in radius and scaling factor ratio $K = 1.1$ for image patch extraction. Potential particles detected as peaks in the DoG map were filtered so that the distance between peaks were at least 10 voxels. 38112 image patches of size 32^3 voxels were extracted for autoencoder network training. In principle, one can also use a sliding window to extract image patches. However, a sliding window on a 3D image would produce a substantially larger amount of image patches that would introduce a substantial larger amount of computational burden.

We randomly split the 38112 image patches into a training set of size 34300 and a validation set of size 3812. The Autoencoder3D model was trained using optimizer Adaptive Moment Estimation (Adam) with exponential decay rates $\beta_1 = 0.9$ and $\beta_2 = 0.99$ to minimize the mean squared error loss function [20]. After one epoch training, the model was saved only if there was an improvement in validation dataset loss compared to previous epoch. Adam training was performed with learning rate 0.001 and a batch size of 8 until the validation dataset loss did not improve for 20 consecutive epochs.

We measured the computation speed of Autoencoder3D network. On average, the training took 0.013s per image patch per epoch for Autoencoder3D. Given the trained Autoencoder3D model, on average, the encoding of an image patch took 0.0012s and the decoding of an encoded image patch took 0.0023s.

3.1.4 K-means clustering of encoded features

After the training, Autoencoder3D network encoded each image patch as a 32 dimension vector. We performed k-means clustering with $k = 100$ on the encoded image patches to group similar image patches together. The cluster center of each group, a 32 dimension vector, was decoded as 3D image patch reconstruction by the Decoder3D network. Figure 3 shows examples of decoded cluster centers.

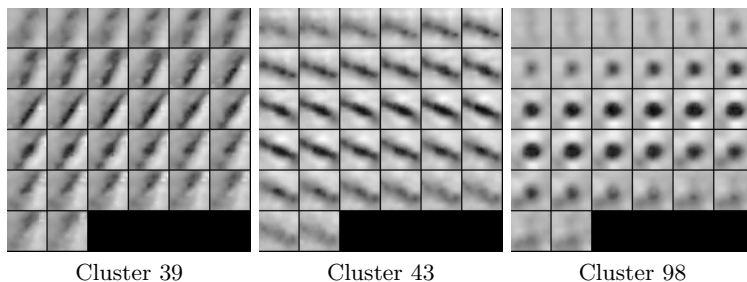


Figure 3: Three decoded cluster centers obtained from COS-7 tomogram 1. 32 images of size 32^2 pixels, each presents a 2D slice of the decoded 3D images, were plotted for each cluster center.

It is evident that clusters 39 and 43 represent parts of surface fragments seen in different orientations. Cluster 98 represents globular particles with sizes similar to that of established ribosomal particles; as such the characteristic structures contained in this cluster are likely ribosomes (termed ribosome-like structures).

After manually labeling these 100 clusters, we selected 10 clusters of 500 image patches that represented surface features of different orientations and 7 clusters of 308 image patches that represented large globular

features. The total 808 image patches of surface and large globular features were used to annotate the COS-7 tomogram 1 (Figure 4). In Figure 4, parts of membrane, carbon edge, and tomogram boundary regions are automatically annotated based on our cluster results. Large globular features that may indicate ribosome-like structures are annotated across a large region in the tomogram.

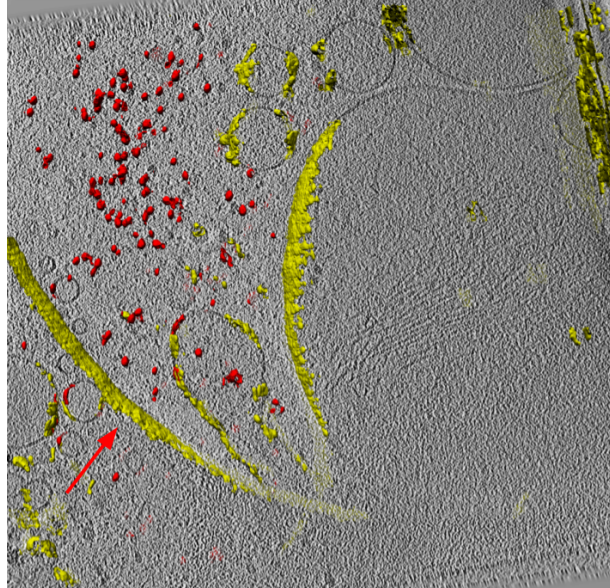


Figure 4: Iso-surfaces of decoded image patches of selected clusters embedded to the COS-7 tomogram 1. Surface features (yellow) and large globular features (red) are annotated in the tomogram. A long carbon edge, annotated in yellow, is indicated by a red arrow.

Image features that may indicate spatial interaction Interestingly, we detected image patches that may indicate spatial interactions between cell components. By visual inspection of the location of the spatial interaction patterns, we found that clusters 6, 64, and 85 represent particles that are enriched in membrane-proximal regions (Figure 5). We averaged the original image patches of each of the three clusters. Figure 5 shows the 2D slices of the averaged image patch of the three clusters of such spatial interaction pattern (Figure 5). We are able to identify a particle in the middle and some spatial interaction (likely to be membrane and particle associations). To better visualize the average image patches of this spatial interaction pattern between membrane and particle, the 2D slices of the images with gaussian smoothing of $\sigma = 3$ are shown in 5. The gaussian smoothed images present clear evidence of such spatial interaction. The decoded cluster centers of these three clusters are also plotted, which provide additional existence evidence of spatial interaction enriched in the membrane regions. The validity and biological implication of this pattern remain to be further investigated.

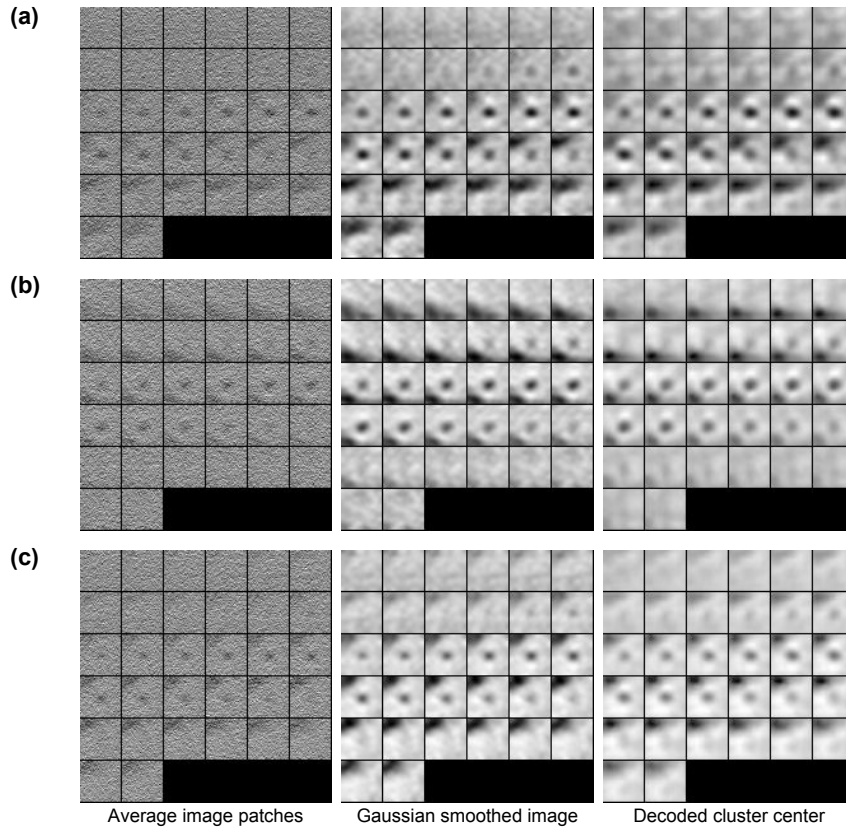


Figure 5: The 2D slices of average image patches of spatial interaction pattern detected in COS-7 tomogram 1. A gaussian smoothed image of $\sigma = 3$ is shown in the middle. The decoded cluster center is shown on the right.

Note that CNN includes pooling layers that introduce a small amount of rotation and translation invariance, therefore the the decoded cluster center has a significantly stronger signal of the membrane than the pure average of the cluster of the original images, which significantly increased the identification ability, as compared to the simple average of the image patches.

3.1.5 Semantic segmentation

Construction of testing dataset from COS-7 tomogram 2 A similar data preparation procedure was carried out on COS-7 tomogram 2. 42097 image patches of size 32^3 voxels were extracted. The image patches were then filtered to reduce the probability of obtaining false-positive results. The 42097 image patches were encoded by the trained Encoder3D network from Section 3.1.3. The 42097 encoded image patches were mapped to its nearest cluster centroid from Section 3.1.4. Only the 312 image patches mapped to surface feature clusters or large globular feature clusters were kept for semantic segmentation. Encodings mapped to other clusters were filtered out as they were less likely to contain any surface or large globular feature. Such filtering can also be performed through our recently developed 3D sub-volume classification approach [43].

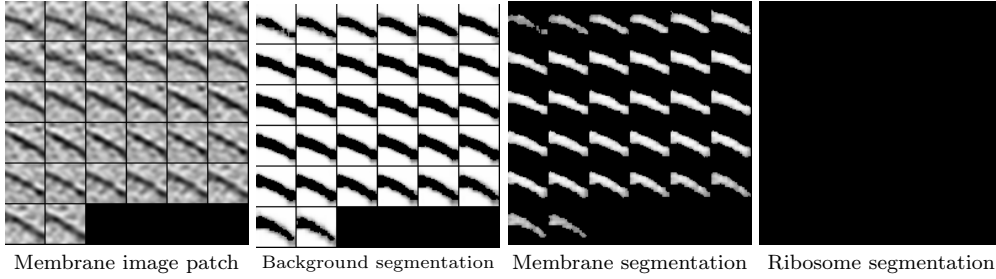


Figure 6: 2D slices of an example image patch (in the COS-7 tomogram 2) being segmented to a surface fragment.

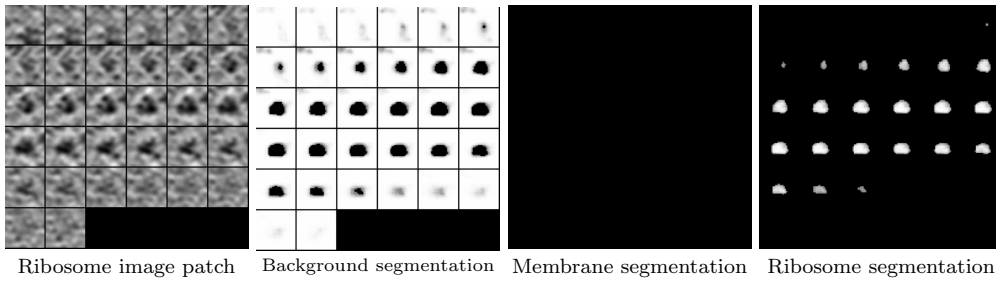


Figure 7: 2D slices of an example image patch (in the COS-7 tomogram 2) being segmented to a large globular.

Construction of training dataset from COS-7 tomogram 1 : We used the k-means clustering results as a training dataset for the Encoder-decoder semantic segmentation network (EDSS3D) and then applied the trained EDSS3D network on the test dataset.

First, the 100 decoded cluster centers were manually labeled with the two most recognizable cellular structures: surface features (membrane, carbon edge, or tomogram boundary) and electron-dense structures with the same general appearance as large globular (termed ribosome-like structures). These structures were grouped as two classes for training. The surface feature class consisted of 10 clusters with 500 image patches in total. And the large globular feature class consisted of 7 clusters with 308 image patches in total. We added a third class, the background class, to denote the background regions where there was no target structure present. The segmentation ground truth was obtained by masking each decoded image patch in the training dataset with level 0.5. Voxels with signal greater than 0.5 were segmented as the background region and voxels with signal less than or equal to 0.5 were segmented as either the surface region or large globular region as determined by the cluster label.

Training : We randomly split the 808 image patches into a training set of size 727 and a validation set of size 81. The encoder-decoder network model was trained using optimizer Adam with exponential decay rates $\beta_1 = 0.9$ and $\beta_2 = 0.99$ to minimize the categorical cross-entropy loss function. After one epoch training, the model was saved only if there was an improvement in validation dataset loss compared with previous epoch. Adam training was performed with learning rate 0.001 and a batch size of 128 until the loss for validation dataset did not improve for 20 consecutive epochs.

Segmentation : The trained EDSS3D network was applied to the testing dataset of 312 image patches. 2D slices of the original testing image patches and the resulting three class segmentation probability results were plotted. Figure 6 and 7 show the segmentation of two example image patches. An overall visual inspection of the segmentation results on the test dataset shows that our unsupervised Autoencoder3D network and weakly supervised EDSS3D network can successfully segment this dataset into semantically meaningful classes and structures.

Figure 8 shows an embedding of segmented image patches to the COS-7 tomogram 2. In figure 8, some membrane regions, including many vesicular membranes, are successfully segmented and annotated in yellow. Carbon edge and tomogram boundary regions were also segmented as surface region in yellow. Large globular features that may indicate ribosome-like structures are segmented and annotated in red across a large region in the tomogram. We note here that only a few image patches were selected after the filtering for semantic segmentation. Some false-negative results were obtained due to the filtering. However, of the selected image patches, surface regions and large globular particles were successfully segmented.

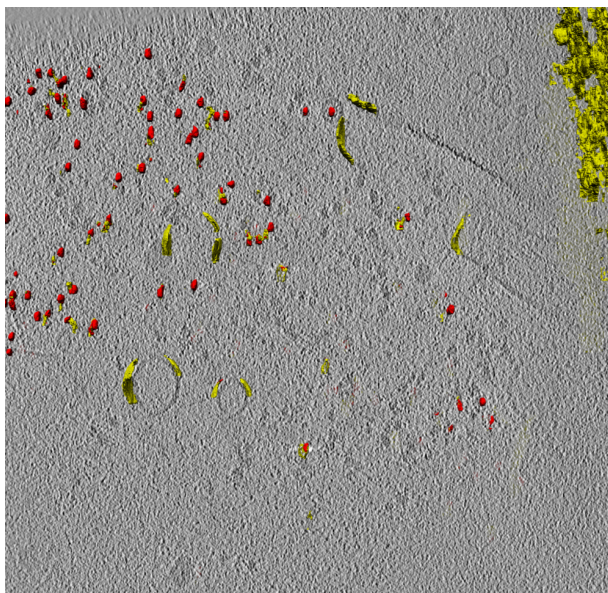


Figure 8: Annotated COS-7 tomogram 2 based on segmentation. Surface feature segmentation (yellow) and large globular particles segmentation (red) are annotated in the tomogram. A tomogram boundary is annotated in yellow on the top right corner.

We measured the computation speed of the EDSS3D network. On average, the training took 0.011s per image patch per epoch. Given the trained EDSS3D model, the segmentation took 0.011s for one image patch.

4 Discussion

CECT has emerged as a powerful tool for 3D visualization of cellular organization at submolecular resolution and at near native state. However, the analysis of structures in a cellular tomogram is difficult due both to the high complexity of image content and to imaging limits. To complement existing approaches, in this paper we proposed a convolutional autoencoder approach for characterizing image features among image patches. We further proposed a weakly supervised semantic segmentation approach by combining convolutional autoencoder and full convolutional network which involves only a very small amount of manual annotation. The preliminary tests of our approaches on experimental cellular cryo-tomograms demonstrate the usefulness of our approaches. This proof-of-principle work presents a useful step towards automatic systematic structural characterization in cellular tomograms.

Potential uses of our method include facilitating *In silico* structural purification and pattern mining in cellular tomograms and tomograms of purified complexes and cell lysate [19], and using selected image feature clusters of the same structure (but possibly in different orientations) to train semantic segmentation. Moreover, template search approaches can also be facilitated by our method. In cases where the user is looking for a specific structure matched to a template, the user can ignore those resulting image patch sets of which their cluster centers are vastly different from the template.

In addition, once the feature clusters are obtained by our Autoencoder3D network, they can then be used to extract/ recognize/ filter/ enhance specific type of image features. Selected image patch clusters grouped by different types of features can be directly used to train a classifier to recognize these features in the similar way as our recent work [43].

In principle, besides convolutional autoencoder, other alternative encoding approaches can also be employed, such as sparse coding [24], dictionary learning [1] and non-local means [8]. However, these alternative approaches do not make use of the inherent structures inside images such as local correlations and hierarchical organization of correlations. In addition, some of these alternative approaches use linear representation models which can be invalid when the linearity assumption is invalid for certain data.

Data preparation and clustering process still require the user to choose proper parameters such as the image patch size, the scale factor of Difference of Gaussian particle picking, and the number of k-means clusters. We provide several visualization method to guide the user to select the optimal parameters. Currently we set an arbitrary number of 100 for clustering. We have tested Gap Statistic [39] and Calinski-Harabasz index [29] for automatically choose the cluster number. Both methods fail to converge to a certain cluster number. Since a simple manual grouping of resulting clusters is required, the impact of cluster number on the results is generally reduced. How to automatically determine cluster number for encoded highly heterogeneous particles from cellular tomograms remains an open problem. In addition, k-means clustering generate different cluster labels for each run, thus the manual selection needs to start over. A more user friendly clustering procedure would be beneficial to further reduce the workload.

Because the image patch clusters selected have limited number of orientations even for same type of structure, the semantic segmentation has limited generalization ability to structures of other orientations. Proper data augmentation techniques, such as rotating or translating image patches, may help for further improving the generalization ability.

5 Acknowledgement

We thank Dr. Robert Murphy for suggestions. We thank Dr. Zachary Freyberg for help with manuscript preparation. We thank Stephanie Siegmund for providing technical help. This work was supported in part by U.S. National Institutes of Health (NIH) grant P41 GM103712. T.Z. acknowledges support of Sir Henry Dale Fellowship jointly funded by the Wellcome Trust and the Royal Society [Grant 107578/Z/15/Z] and Wellcome Trust Joint Infrastructure Fund Award 060208/Z/00/Z and Wellcome Trust Equipment Grant 093305/Z/10/Z to the Oxford Particle Imaging Centre.

References

- [1] Dictionary learning. *IEEE Signal Processing Magazine*, 28(2):27–38, 2011.
- [2] Martín Abadi, Paul Barham, Jianmin Chen, Zhifeng Chen, Andy Davis, Jeffrey Dean, Matthieu Devin, Sanjay Ghemawat, Geoffrey Irving, Michael Isard, et al. Tensorflow: A system for large-scale machine learning. *arXiv preprint arXiv:1605.08695*, 2016.
- [3] Charu C Aggarwal, Alexander Hinneburg, and Daniel A Keim. On the surprising behavior of distance metrics in high dimensional space. In *International Conference on Database Theory*, pages 420–434. Springer, 2001.
- [4] Vijay Badrinarayanan, Alex Kendall, and Roberto Cipolla. Segnet: A deep convolutional encoder-decoder architecture for image segmentation. *arXiv preprint arXiv:1511.00561*, 2015.
- [5] A. Bartesaghi, P. Sprechmann, J. Liu, G. Randall, G. Sapiro, and S. Subramaniam. Classification and 3D averaging with missing wedge correction in biological electron tomography. *Journal of structural biology*, 162(3):436–450, 2008.
- [6] Alberto Bartesaghi, Guillermo Sapiro, and Sriram Subramaniam. An energy-based three-dimensional segmentation approach for the quantitative interpretation of electron tomograms. *IEEE Transactions on Image Processing*, 14(9):1314–1323, 2005.

- [7] M. Beck, V. Lui, F. Förster, W. Baumeister, and O. Medalia. Snapshots of nuclear pore complexes in action captured by cryo-electron tomography. *Nature*, 449(7162):611–615, 2007.
- [8] Priyam Chatterjee and Peyman Milanfar. A generalization of non-local means via kernel regression. In *Computational Imaging Vi*, page 68140, 2008.
- [9] Muyuan Chen, Wei Dai, Ying Sun, Darius Jonasch, Cynthia Y He, Michael F Schmid, Wah Chiu, and Steven J Ludtke. Convolutional neural networks for automated annotation of cellular cryo-electron tomograms. *arXiv preprint arXiv:1701.05567*, 2017.
- [10] Yuxiang Chen, Thomas Hrabe, Stefan Pfeffer, Olivier Pauly, Diana Mateus, Nassir Navab, and F Forster. Detection and identification of macromolecular complexes in cryo-electron tomograms using support vector machines. In *Biomedical Imaging (ISBI), 2012 9th IEEE International Symposium on*, pages 1373–1376. IEEE, 2012.
- [11] Yuxiang Chen, Stefan Pfeffer, José Jesús Fernández, Carlos Oscar S Sorzano, and Friedrich Förster. Autofocused 3d classification of cryoelectron subtomograms. *Structure*, 22(10):1528–1537, 2014.
- [12] François Chollet. keras. <https://github.com/fchollet/keras>, 2015.
- [13] Javier Collado and Rubn Fernndez-Busnadiego. Deciphering the molecular architecture of membrane contact sites by cryo-electron tomography . *Biochimica et Biophysica Acta (BBA) - Molecular Cell Research*, 2017.
- [14] Lidia Delgado, Gema Martínez, Carmen López-Iglesias, and Elena Mercadé. Cryo-electron tomography of plunge-frozen whole bacteria and vitreous sections to analyze the recently described bacterial cytoplasmic structure, the stack. *Journal of structural biology*, 189(3):220–229, 2015.
- [15] Zachary Frazier, Min Xu, and Frank Alber. Tomominer and tomominer cloud: A software platform for large-scale subtomogram structural analysis. *Structure, in press*, 2017.
- [16] Ian Goodfellow, Yoshua Bengio, and Aaron Courville. *Deep Learning*. MIT Press, 2016. <http://www.deeplearningbook.org>.
- [17] Kay Gr̃unewald, Prashant Desai, Dennis C Winkler, J Bernard Heymann, David M Belnap, Wolfgang Baumeister, and Alasdair C Steven. Three-dimensional structure of herpes simplex virus from cryo-electron tomography. *Science*, 302(5649):1396–1398, 2003.
- [18] Marion Jasnin, Mary Ecke, Wolfgang Baumeister, and Günther Gerisch. Actin organization in cells responding to a perforated surface, revealed by live imaging and cryo-electron tomography. *Structure*, 24(7):1031–1043, 2016.
- [19] Simon Kemmerling, Stefan A Arnold, Benjamin A Bircher, Nora Sauter, Carlos Escobedo, Gregor Der-nick, Andreas Hierlemann, Henning Stahlberg, and Thomas Braun. Single-cell lysis for visual analysis by electron microscopy. *Journal of structural biology*, 183(3):467–473, 2013.
- [20] Diederik Kingma and Jimmy Ba. Adam: A method for stochastic optimization. *arXiv preprint arXiv:1412.6980*, 2014.
- [21] Alex Krizhevsky, Ilya Sutskever, and Geoffrey E Hinton. Imagenet classification with deep convolutional neural networks. In *Advances in neural information processing systems*, pages 1097–1105, 2012.
- [22] Yann LeCun, Yoshua Bengio, and Geoffrey Hinton. Deep learning. *Nature*, 521(7553):436–444, 2015.
- [23] Yann LeCun, Léon Bottou, Yoshua Bengio, and Patrick Haffner. Gradient-based learning applied to document recognition. *Proceedings of the IEEE*, 86(11):2278–2324, 1998.
- [24] Honglak Lee, Alexis Battle, Rajat Raina, and Andrew Y Ng. Efficient sparse coding algorithms. In *International Conference on Neural Information Processing Systems*, pages 801–808, 2006.

- [25] Jonathan Long, Evan Shelhamer, and Trevor Darrell. Fully convolutional networks for semantic segmentation. In *Proceedings of the IEEE Conference on Computer Vision and Pattern Recognition*, pages 3431–3440, 2015.
- [26] Imanol Luengo, Michele C Darrow, Matthew C Spink, Ying Sun, Wei Dai, Cynthia Y He, Wah Chiu, Tony Pridmore, Alun W Ashton, Elizabeth MH Duke, et al. Survos: Super-region volume segmentation workbench. *Journal of Structural Biology*, 198(1):43–53, 2017.
- [27] A. Martinez-Sanchez, I. Garcia, and J.J. Fernandez. A differential structure approach to membrane segmentation in electron tomography. *Journal of Structural Biology*, 175(3):372–383, 2011.
- [28] Antonio Martinez-Sanchez, Inmaculada Garcia, and Jose-Jesus Fernandez. A ridge-based framework for segmentation of 3d electron microscopy datasets. *Journal of structural biology*, 181(1):61–70, 2013.
- [29] Ujjwal Maulik and Sanghamitra Bandyopadhyay. *Performance Evaluation of Some Clustering Algorithms and Validity Indices*. IEEE Computer Society, 2002.
- [30] Vinod Nair and Geoffrey E Hinton. Rectified linear units improve restricted boltzmann machines. In *Proceedings of the 27th international conference on machine learning (ICML-10)*, pages 807–814, 2010.
- [31] Andrew Ng. Sparse autoencoder. *CS294A Lecture notes*, 72(2011):1–19, 2011.
- [32] Fabian Pedregosa, Gaël Varoquaux, Alexandre Gramfort, Vincent Michel, Bertrand Thirion, Olivier Grisel, Mathieu Blondel, Peter Prettenhofer, Ron Weiss, Vincent Dubourg, et al. Scikit-learn: Machine learning in python. *The Journal of Machine Learning Research*, 12:2825–2830, 2011.
- [33] Long Pei, Min Xu, Zachary Frazier, and Frank Alber. Simulating cryo electron tomograms of crowded cell cytoplasm for assessment of automated particle picking. *BMC bioinformatics*, 17(1):405, 2016.
- [34] E.F. Pettersen, T.D. Goddard, C.C. Huang, G.S. Couch, D.M. Greenblatt, E.C. Meng, and T.E. Ferrin. UCSF Chimera visualization system for exploratory research and analysis. *Journal of computational chemistry*, 25(13):1605–1612, 2004.
- [35] Prabhu Ramachandran and Gal Varoquaux. Mayavi: 3d visualization of scientific data. *Computing in Science & Engineering*, 13(2):40–51, 2011.
- [36] A. Rigort, D. Günther, R. Hegerl, D. Baum, B. Weber, S. Prohaska, O. Medalia, W. Baumeister, and H.C. Hege. Automated segmentation of electron tomograms for a quantitative description of actin filament networks. *Journal of Structural Biology*, 2011.
- [37] S.H.W. Scheres, R. Melero, M. Valle, and J.M. Carazo. Averaging of electron subtomograms and random conical tilt reconstructions through likelihood optimization. *Structure*, 17(12):1563–1572, 2009.
- [38] Guang Tang, Liwei Peng, Philip R Baldwin, Deepinder S Mann, Wen Jiang, Ian Rees, and Steven J Ludtke. Eman2: an extensible image processing suite for electron microscopy. *Journal of structural biology*, 157(1):38–46, 2007.
- [39] Robert Tibshirani, Guenther Walther, and Trevor Hastie. Estimating the number of clusters in a data set via the gap statistic. *Journal of the Royal Statistical Society*, 63(2):411–423, 2001.
- [40] M. Xu, M. Beck, and F. Alber. High-throughput subtomogram alignment and classification by Fourier space constrained fast volumetric matching. *Journal of Structural Biology*, 178(2):152–164, 2012.
- [41] M. Xu, S. Zhang, and F. Alber. 3d rotation invariant features for the characterization of molecular density maps. In *2009 IEEE International Conference on Bioinformatics and Biomedicine*, pages 74–78. IEEE, 2009.
- [42] Min Xu, Martin Beck, and Frank Alber. Template-free detection of macromolecular complexes in cryo electron tomograms. *Bioinformatics*, 27(13):i69–i76, 2011.

- [43] Min Xu, Xiaoqi Chai, Hariank Muthakana, Xiaodan Liang, Ge Yang, Tzviya Zeev-Ben-Mordehai, and Eric Xing. Deep learning based subdivision approach for large scale macromolecules structure recovery from electron cryo tomograms. *ISMB/ECCB 2017, Bioinformatics (in press); arXiv preprint arXiv:1701.08404*, 2017.
- [44] Min Xu, Elitza I Tocheva, Yi-Wei Chang, Grant J Jensen, and Frank Alber. De novo visual proteomics in single cells through pattern mining. *arXiv preprint arXiv:1512.09347*, 2015.
- [45] Xiao Ping Xu, Christopher Page, and Niels Volkman. *Efficient Extraction of Macromolecular Complexes from Electron Tomograms Based on Reduced Representation Templates*. Springer International Publishing, 2015.